http://sure.sunderland.ac.uk/policies.html or alternatively contact sure@sunderland.ac.uk.

Fabrication of Photo-electrochemical biosensor for ultrasensitive screening of mono-bioactive molecules in living cells

N. Akhtar[a,b], M. Emran[a], M. A. Shenashen[a], H. Khalifa[a], T. Osaka[b], A. Faheem[c], T. Homma[b], H. Kawarada[b*], S. A. El-Safty[a,b,*]

The controlled design of biosensors based on photo-electrochemical technique with high selectivity, sensitivity, and rapid response for monitoring of mono-bioactive molecules, particularly dopamine (DA) levels in neuronal cells is highly necessary for clinical diagnosis. Hierarchical carbon-, nitrogen-doped (CN) nickel oxide spear thistle (ST) flowers associated in single-head (S), and symmetric and asymmetric-double heads (D, and A, respectively) that tightly connected through micrometric dipole-like rod or trunk were fabricated by using a simple synthetic protocol. The CN-ST flower heads were decorated with dense nano-tubular like hedgehog needless skins in vertical alignments. These designated architectures are key features for creating biosensor surface electrodes for photo-electrochemical, ultrasensitive screening of mono-bioactive molecules. The exceptional electrode designs produced numerous catalytically active sites, large surface area, and high electron-transfer mobility. The active coating of carbon-nitrogen nanospheres significantly enhanced the photo-electrocatalytic activity of the prepared bio-sensor electrodes and prevented leakage of photocatalytic activity under long- term exposure of irradiation. Among all photo-electrochemical assays, the biosensors showed significant sensitivity and selectivity of DA in the presence of interfered molecules such as ascorbic acid (AA), uric acid (UA), adrenaline (A), and noradrenaline (NA). The photo-electrochemical CN-SST electrode biosensor showed significant sensing performance of DA in terms of unimpeded diffusion pathways, a wide concentration-detection range, and a low detection limit of up to 6 nM, even in the coexistence of the potentially interfering molecules compared with other CN-DST and CN-AST electrodes. Furthermore, the photo-biosensor electrode shows potential in the selective and sensitive determination of DA from living cells (PC12). This finding indicates that the hierarchical ST biosensor may enable analytical discrimination and monitoring of DA secreted from living cells for clinical diagnosis application.

1- Introduction

The ability of the human body to regulate the variables at steady or stable internal environment is known as homeostasis.[1] The health of a human body is highly dependent upon the functioning of the organs to maintain homeostasis by regulating various negative and positive feedback mechanisms.[1] The slight inability in organs to regulate the stable internal environment may lead to serious health problems or even death. Significant progress has been created to assist in the detection of various abnormalities in the human body by control monitoring of several bio-molecules such as dopamine, uric acid (UA), ascorbic acid (AA), glucose, and hydrogen peroxide (H_2O_2). The precise detection of these biomolecules would have the ability to provide useful information about the treatment and prevention of various genetic problems.[2] Therefore, keen interest has grown in developing portable sensor for rapid, cost effective and on-site monitoring of wide range of targets to revolutionize scientific research. Dopamine is an important catecholamine neurotransmitter in the mammalian central nervous system where it plays a key role in controlling locomotion, learning, working memory, cognition, and emotions.[3] Several neurological disorders, including Parkinson's disease, schizophrenia, human immunodeficiency virus infection, and restless leg syndrome resulted from the abnormality in the dopamine concentrations.[3,4] Therefore, finding a reliable

[a] National Institute for Materials Science (NIMS), Research Center for Functional Materials, 1-2-1 Sengen, Tsukuba-shi, Ibaraki-ken, 305-0047, Japan.
[b] Graduate School for Science and Engineering, Waseda University, 3-4-1 Okubo, Shinjuku-ku, Tokyo 169-8555, JAPAN.
[c] School of Pharmacy and Pharmaceutical Sciences, Faculty of Health Sciences and Wellbeing, University of Sunderland, Sunderland, SR1 3SD, UK
† E-mail: sherif.elsafty@nims.go.jp & kawarada@waseda.jp
Electronic Supplementary Information (ESI) available: [characterization analysis apparatus, schematic preparation of materials, SEM for the prepared materials, XPS spectrum with survey of N1 2P and O 1S, DPV for AA, DA and UA at ITO and CN-SST individual and simultaneous detection of AA, DA and UA using DPV, amperometric response for DA released form PC12 and the column for obtaining the current response with and without PC12, and column plot for discovery of stability and reproducibility.]. See DOI: 10.1039/x0xx00000x

analytical method is clinically important to measuring dopamine level in physiological or biological samples.

Several methods have been reported and developed to quantitatively detect dopamine using simple instruments such as Raman spectroscopy, capillary electrophoresis, fluorescence spectrometry and high-performance liquid chromatography.[4, 5] However, most such sensing devices cannot compete with the electrochemical method due to its advantages of low cost, simple operating system, high sensitivity and commercial availability to the public. Electrochemical dopamine sensors with enzymes (e.g., tyramine oxidase) play a leading role in research attempts to simplify dopamine testing and are expected to play a similar role in the move toward continuous dopamine monitoring.[6] However, the major disadvantages of these enzymatic dopamine sensors are their lack of stability, difficulty of recycling, and tedious fabrication processes, which are hard to overcome. Consequently, substantial attention has been focused on direct electrocatalytic oxidation of dopamine at enzyme-free electrodes with high sensitivity and stability, fast response time, simple fabrication process, and wide working range.

A major challenge in using non-enzymatic electrochemical sensor for the precise monitoring of dopamine is to find a material that can accurately sense dopamine in the co-existence of high concentration of primary interferences such as UA and AA.[7] To overcome these challenges, two fundamental approaches have been developed: one is to pre-coat the working electrode surface with negatively charged polymer such as nafion. This negatively charged polymer repels the anionic species such as UA and AA, while attracting the positively charged dopamine.[8] However; these negatively charged polymer-based electrodes suffer from drawbacks such as very low sensitivity, poor reproducibility and non-uniform thickness. The second approach is to modify the electrode surface by applying a variety of advanced nanostructures/microstructures with well-controlled shape that can separate the oxidation potential of dopamine from UA and AA.[9] Thus far, intensive efforts have been devoted to modify the electrode surface with various structures including gold nanowires, nanoslices and nanocorals, palladium nanoclusters, CuO nanoleafs, titanium dioxide nanosheets and reduced graphene oxide sheets modified with gold nanoparticles, [10–14] NiCo-NPs-in-N/C, graphene fiber, and reduced graphene oxide-zinc oxide are used for simultaneous detection of AA,UA, and DA wherein the detection limits were 0.091, 0.08, and 0.014; 50, 0.1, and 0.2; 3.7, 0.33, and 1.08; respectively.[15–17] However, most of these structural modifications provide high selectivity but lack sensing efficiency. Therefore, constructing electrochemical dopamine sensor is particularly challenging for designing nanostructures/microstructures with controlled shape that can preferentially expose a great fraction of electrochemically active sites to achieve high sensitivity and selectivity.

Photo-electrochemistry possesses different form of excitation energy (light) and detection, thus it is representing high sensitive analytical method. Furthermore, the use of electronic detection turned the photo-electrochemical (PEC) instrument easier and low cost compared with conventional optical methods. Although photo-electrochemistry is a potentially sensitive analytical method, limited material has photoactive property for photo-electrochemical application. [18,19]

Transition metal oxides have characteristic properties, such as size-tunable optical and electronic properties; therefore, it is used in the field of PEC.[20–22] However, transition metal oxides optical properties have limitations in instability and photo corrosion. [23,6]

Hence, to overcome these problems, carbonaceous materials (such as graphene, carbon nanotubes, and carbon dots) were used as dopant materials to enhance the visible light PEC properties and prevent the photo corrosion of the transition metal oxides.[24–30] Improvement of ZnO NPs efficient of energy in visible light was achieved after doping ZnO NPs on functionalized SWCNTs.[29] In addition, graphene enhances the photocurrent enhancement of TiO_2 nanocrystals under visible light as reported, which was five times higher than that of only TiO_2 nanocrystals.[27] All these above-mentioned results indicate that the PEC properties of transition metal oxides can be improved effectively by appropriate doping with carbonaceous materials, and designing various attempts to prepare novel carbonaceous material-doped semiconductor nanohybrids for PEC sensing under visible light is still highly desirable and technologically important.

A few reports for PEC biosensors, such as graphene quantum dots–TiO_2 nanocomposite, were developed for dopamine sensing under visible light irradiation with low detection limit and wide linear range.[30] Other PECs using composite materials (metal oxides with carbonaceous materials) were reported for glucose, NADH, and H_2O_2 sensing.[31–35]

In this study, photo-electrochemical biosensor was fabricated based on hierarchical carbon-, nitrogen-doped (CN) nickel oxide spear thistle (ST) flowers associated in single-head (S), and symmetric and asymmetric-double heads (D, and A, respectively) that tightly connected through micrometric dipole-like rod or trunk. The significant enhancement of photo-electrochemical performance for monitoring of mono-bioactive molecules, particularly dopamine (DA) levels in neuronal cells was due to the morphological CN-ST architectures. The CN-ST flower heads were decorated with dense nano-tubular like hedgehog needless skins in vertical alignments. The CN-ST structural ordination and arrangement lead to exceptional electrode designs with numerous catalytically active sites, large surface area, and high electron-transfer mobility. In addition, the CN nanosphere- doped ST acts as electron transport channels between the active centers of the electrode–electrolyte interface, leading to enhanced stabilization photo electrocatalytic activity of CN-ST biosensors under irradiation. The CN-ST biosensors show real evidence of control photo-electrochemical detection of wide-range bioactive-molecules. Furthermore, the CN-ST design can selectively monitor DA in living cells in a specific biosensing protocol. Among all of geometrical structures of CN-ST photo-biosensor electrodes, the CN-SST biosensor shows high photo-

electrocatalytic activity, leading to create DA-sensitive and -selective sensing assays. Significantly, the determination of DA released from living cell (PC12) was successfully achieved with potential sensitivity and selectivity using CN-SST biosensor. This finding indicates that the hierarchical CN-SST based photo biosensor may enable monitoring of DA secreted from living cells.

Scheme1

2- Results and discussion

Controlling growth with directing morphology of NiO was assembled. Construction of NiO was built depending on the morphology directing agent diammonium hydrogen phosphate ($(NH_4)_2HPO_4$). Controlling addition of directing agent with constant flow rate (Q) forming different constructions of NiO like spear thistle (ST) flowers with (single head (S), symmetric double head (D)and asymmetric double head (A) that tightly connected through micrometric dipole-like rod or trunk as in scheme S1. The initial precursor nickel nitrate hexahydrate ($Ni(NO_3)_2.6H_2O$, $(NH_4)_2HPO_4$) and the as-obtained (ST) flowers construction can produce from successive reactions. In a typical procedure, hydrolysis of $(NH_4)_2HPO_4$ produce OH^- anions, which subsequently reacted with Ni^{2+} to form Ni-OOH ST hierarchy. The dropwise addition of PO_4^{3-} ions to the composition domains in definitely-controlled follow rate leads to control the formation of ST flower structure associated in single-head (S), and symmetric and asymmetric-double heads (D, and A, respectively), see Scheme S1.

The ST crystal growth with controlling head shapes may be due to the electrostatic attraction between positive and negative charge, where PO_4^{3-} ions possess a massive negative charge and attracted the Ni^{2+} ions. Thus, PO_4^{3-} ions are the key role in the formation of hierarchal architectures (SST, DST and AST). The flow rate of additive $NH_4)_2HPO_4$ directly affected the kinetic growth and shape of ST heads. Moreover, the ST head construction may be attributed to the stereo PO_4^{3-} shape in its solution, which reflected to the crystal growth depth from inner to outer. CN was assembled after stable construction of ST, a thin film for poly-aniline that polymerized at 0°C after dropwise addition of potassium persulfate with continuous stirring. Potassium persulfate starts the free radical monomer, with continued homogenous black precipitate was formed at ST surfaces. Carbonization of polyaniline that acts as the nitrogen and carbon source at 500 °C in Ar gas flow revealed a homogenous CN that dressed at the surface of ST samples.

2.1 Structure features of ST hierarchal biosensor

Fig. 1A shows the high-angle-annular-dark-field scanning transmission electron microscopy (HAADF-STEM) of ST with Symmetric double head (D), wherein two heads spread in opposite sides and tightly connected through micrometric dipole-like rod or trunk. High-magnification HAADF-STEM image (Fig. 1B) represents ST flower heads were decorated with dense nano-tubular like hedgehog needless skins in vertical alignments. High magnification focused on the head surface clearly reflects the surface contains a thick nanotube at the head surface ends with average size of 15–20 nm as in Fig. 1C. As shown in Fig. 1D, the whole head of ST samples is uniformly covered with carbon nanosphere with an average size of 5-10 nm. High-magnification HAADF-STEM image (Fig. D) shows that C spheres with an average thickness of less than 10 nm have been oriented along the nanotube-like morphology.

Confirmation of the distribution and elemental contents at the surface of ST was demonstrated by EDS-STEM mapping as in Figs. 1(E–I). The surface elemental composition and distribution reflect the homogeneous distribution of C, Ni, O, and N at the CN-ST samples and dominant Ni and O atoms with high percentage, such as 46.2% and 48.05% for Ni and O, respectively, also revealed that the carbon present on the surface contains 4.15% and small amount of doping N (1.6%). These results provide the surface containing carbon and nitrogen-ST with homogeneous distribution that is responsible for the smooth surface of ST and the pore distribution at the surface. ED-STEM can provide the crystalline degree of the active surface as in Figs. 1(K–M), which reflects the highly order crystalline surface with different active planes for DST-AST, and SST, namely, (111), (101), and (110), respectively. ED-STEM image of nanotubes at the surface of DST-AST, and SST reflects that the crystal growth is grown along {111}, {101}, and {110} facets, respectively. Figs. 1(N–P) shows the SAED-TEM images that revealed the diffraction spots around [111], [101], and [110] crystal facet planes.

Further confirmation of controlled structure was obtained from field emission- scanning electron microscope (FE-SEM) images as in Fig. S1. Fig. S1A shows the homogeneous and unit geometrical structure of ST flower like, which is similar to spear thistle (SST) flowers with single head and trunk. High magnification of FE-SEM reflects that the head size was approximately 3–4 µm with trunk size of approximately 1–2 µm, and relevant CN covers the unite surface (Fig. S1A, inset). After the flow rate was defined, ST was constructed with double head connected by trunk in-between and the two heads spread in opposite sides like dipole with symmetric double head (DST) (Fig. 1SB) and asymmetric double head (AST) (Fig. S1C). Construction of ST with asymmetric double head and CN was revealed from inset Fig. S1C, where and C-nitrogen nanospheres covers the surface of NiO with homogeneity of formality.

High resolution- Transmission electron microscope (HR-TEM) images further revealed that the hierarchical ST doped with CN was grown. The Findings obtained from TEM, EDS-STEM, and SEM profiles (Fig. 1), CN were uniformly bound on the whole surface of prepared materials through the H-bonding or electrostatic interactions preferably rearranged to form well-dispersed and homogeneous CN nanoparticles (<<10 nm).

Figure1

Active sites for {110}, {101}, and {111} crystal planes and its surface atomic configurations, electron density difference maps, and pulse surface electrons in continuous generation modes around ST are illustrated by density functional theory (DFT) (Fig. 2). Double layer atomic configuration of Ni^{2+} and O^{2-}

around {111} crystal plane of SST provides the highly crystalline order of its surface and alignment of atomic distribution (A). The mesostructured pore windows formed around {110} SST crystal facet with center cubic fm3m crystal symmetry were taken perpendicular to the fourfold axis and with tilt modelling to show a pronounced atomic-scale arrangement at the center and edge of the crystal lattice along the entire tube-shaped layer. Open pores at the ends of the nanotubes of SSH directly affected on the electro-catalytic nature by influencing the charge transfer and mass transport, leading to rapid strong binding with the target molecules. The contact surface was further provided with target molecules with active sites Ni^{2+} and rich-O^{2-} vacancies along with the atomic monolayer based on axial alignment, which affects the catalytic behavior of {110} plane as in Fig. 2B. The continuous electron streams of double layer on the top-level isosurface of the {111} and {101} orientations of DST and AST distributed closely to a central and focal point surface around Ni^{2+} and O^{2-} vacancy sites (Figs. 2C and 2D). The difference of crystal planes of ST because of variable geometrical shape along with atomic configuration around each crystal planes, which represents the effectiveness of catalytic activity of each surface, the power of binding with target biomolecules, and centered active atoms. The atomic configuration and charge surface were affected by the presence of CN at its surface, where a cloud of charge around {110} plane for single layer of Ni^{2+} and rich-O^{2-} configuration (E). The surface charge characteristic of Ni^{2+} and rich-O^{2-} vacancies configuration was influenced by CN. the clouds of CN cover the surface, where the stability of dominant rich-O^{2-} vacancy sites increased. The partial polarization between N and C stabilizes and enhances the O^{2-} vacancy sites and increases the binds with positively target biomolecules, such as DA. Photo-corrosion of ST biosensor decreased as the presence of CN that is similar to a protective layer and represents as a negative charge balancers. The surface-representing localized networks of the confinement electrostatic potential and elevated the surface charge density around C, N, O, and Ni atoms and effective potential DA-to-Ni^{2+} site binding. This geometric molecule-to-surface orientation generated numerous accessible surface sites, flexible interactions, and thermodynamically stable bindings. The surface configurations of hierarchical SST oriented with nanotubes with open holes and longitudinal long-range channels can feasibly create dense Ni^{2+} atoms and more electron-rich O^{2-} vacancy sites, producing more efficient electron transport. CN facilitates the mass transport and effectiveness for binding of target molecule at {110} exposed plane.

Figure 2

N_2 adsorption−desorption isotherm was used for detection of surface area and pore size distribution. As shown in Fig. 3A the N_2 adsorption isotherms exhibit IV feature with H1 hysteresis loop. Hysteresis between adsorption and desorption branches observed at 0.82 <p/p0>1 for CN-SST and form at 0.88 <p/p0>1 for CN-DST and CN-AST whereas form at 0.92 <p/p0>1 for SST, which demonstrated the hierarchical formation of ST architectures. CN has potentially effect in the surface area and porous structure .[35,36] Pore-size distribution was observed according to the NLDFT model (Fig. 3B), where the dominant porous structure was in the region of mesoporous. All the samples displayed very close pore size distribution, and CN-SST exhibits the highest pore volume. The specific surface areas of S_{BET} = 22.3, 42.3, 60.5, and 75.4 $m^2 g^{-1}$ for SST (a) CN-DST (b), and CN-AST (c), CN-SST (d) respectively. Significant increasing of the surface area increases in the presence of CN for SST (table inset Fig. 3B), which prevent the agglomeration of the ST. CN-SST has the highest surface area and provides an invasive electrolyte electrode interface and can enhance the ion diffusion kinetics. Consequently, structure formation can improve the photo-electrochemical capacitance and the charge transfer kinetics.

Sharp and well-resolved diffraction peaks for the ST samples are found in the WA-XRD patterns as shown in Fig. 3C, which was consistent with JCPDS no. 01-089-5881 (i.e., a face-centered cubic Fm3m symmetry with the lattice constant α = 8.35 Å). However, WA-XRD profile of carbon incorporated SST, DST and AST (Fig. 3C-b) were found to keep the characteristic diffraction peaks of face-cantered cubic NiO (JCPDS no. 01- 089-5881), along with a broad peak at 2Θ = 24.61, indicating the existence of carbon. Raman spectra can provide characteristic features of sample molecules that act as fingerprint, unique to a molecule or indeed and individual molecular structure. The Raman spectra of the SST, DST, and
AST samples show several bands above 400 cm^{-1} at an excitation wavelength of 532 nm as in Fig. 3A. The Raman spectra of SST, DST, and AST showed a vibrational band at approximately 532, 750, and 1085 cm^{-1} caused by (1P) and (2P) corresponding to the first-order transverse optical TO, 2TO, and 2LO (longitudinal optical) modes, respectively, which are characteristics for NiO.[37] However, the existence of two distinct peaks in CN-SST, CN-DST and CN-AST corresponds to D (~1350 cm^{-}) and G (~1600 cm^{-1}) bands originating from the disordered carbon and sp^2 cluster, respectively.[38] To elucidate the surface features and components of CN-doped ST compared, ST measurements were performed. Fig. S2A shows wide range XPS spectra (i.e., survey) of ST and CN doped ST components. In addition, high-resolution XPS spectra of C 1s and N 1s peaks are shown in Figs. 3E and 3F, respectively. Fig. 3E shows high-resolution XPS spectra of the C 1s peaks to reveal the carbon source in ST, which represents strong peaks at 285.01, 285.8, 288.2, and 289.4 eV assigned to C-C (sp_2), C-C (sp3), C=O, and O-C=O bands, respectively, indicating the conversion of poly-aniline to CN nanospheres after carbonization. The presence of pyridinic nitrogen that results from the defects caused by N-doping may enable the analyte to penetrate more rapidly and boost the shuttling of ions at the electrode–electrolyte interface.[39] The N1s spectra with four main peaks centered at 398.22, 399.14, 400.4, and 402.6eV assigned to pyridinic nitrogen (C=N), pyrrolic nitrogen (C-N), graphitic nitrogen, and N-oxide of pyridinic nitrogen, respectively, as in Fig. 3F. The Ni 2p spectra with main peaks centered at 872.3 and 854.3 eV assigned to Ni 2p1 and Ni 2p3 of Ni (II) ions, respectively.[40] The peaks of Ni 2p and O 1s in the

ST undergo visible shifts to lower binding energy compared with pristine ST (Figs. S2B and S2C). This finding indicates the surface binding interactions between the C N nanospheres and ST.

Figure 3

2.2 Photo-electrocatalytic activity of CN-ST biosensor

First, the photo-electrochemical behaviors of the NiO-based (such as DST, AST, and SST), and CN-NiO-based biosensors (such as CN-DST, CN-AST, and CN-SST) deposited at ITO electrode were investigated using cyclic voltammetry in 0.1 M phosphate buffer solution (PBS) (pH 7.4) containing 1 mM $[Fe(CN)_6]^{3-}$ within the potential range of 0.0 V to 0.6 V (vs. Ag/AgCl) at a scan rate of 100 mV/s (Fig. 4A). $[Fe(CN)_6]^{3-}$ was used as a redox probe to investigate various factors, including electronic properties, surface structure, and surface chemistry that affect charge kinetics of the selected electrodes. As shown in Fig. 4A, the redox peak separation (ΔEp) values of the CN-DST (95 mV), CN-AST (80 mV), and CN-SST (60 mV) photo-biosensor electrodes were significantly lower than that of the DST (120), AST (100 mV), and SST (90 mV) photo-biosensor electrodes, which can be attributed to the enhanced ion transmission performance at the electrode–electrolyte interface, thereby engaging greater fractions of catalytic active sites at the surface of the electrode for the Faradaic redox reaction.[41]

To investigate the effect of ST geometrical structure, and CN-doped ST electrode designs on the photo-electrochemical oxidation activity of DP molecule, we study the C.V of the NiO-based (such as DST, AST, and SST), and CN-NiO-based (such as CN-DST, CN-AST, and CN-SST) photo-biosensor electrodes in 0.1 M PBS at pH=7, 5 µM DA at a scan rate of 100 mvs^{-1} under UV (362 nm) light irradiation, respectively. Fig. 4B shows that the photocatalytic current of SST photo-biosensor electrode with CN is higher than that of pristine NiO electrode. SST photo-biosensor electrode exhibiting negative shift compared with the other samples may be due to its high surface area, pore volume, and effective faceted {110} plane due to highly dense active sites and atomic configuration of Ni^{2+} and O^{2-} as presented in Scheme 1.

Interfacial electron-transfer rate was measured using EIS to decouple the electrocatalytic activity of the ST-, and CN-ST photo-biosensor electrodes. In an EIS measurement, the semicircle diameter reflects the electron-transfer resistance (*Ret*) of the electrode, and the line reflects the diffusion of the electroactive species. In general, a large semicircle indicates a high charge transfer resistance of the electrode, implying a low electron transfer rate (higher resistivity). Typical Nyquist impedance plots of ST-, and CN-ST photo-biosensor electrodes in 0.1 M PBS (pH 7.4) are shown in Fig. 4C. The SST-based photo-biosensor structures (Fig. 4C) represent a small semicircle diameter at high frequency, showing a relatively small *Ret*. The semicircle of the CN-SST photo-biosensor electrode showed further decrease, with extremely lower *Ret* value and higher conductivity than that of SST electrodes. This finding suggests the enhanced electron-transport efficiency of the CN-SST photo-biosensor. Furthermore, the key parameters of CN-SST photo-biosensor such as high surface area, dominant {110} crystal facet play role in the low resistivity, high electron diffusion pathway, and high DA-sensitivity electrode design compared with the other CN-DST and CN-AST structures.

The effect of solution pH on the photo-electrochemical oxidation of 5 µM DA on CN-SST photo-biosensor electrode was investigated in the range of 6 to 9 at a scan rate of 100 mVs^{-1} by time-dependent on–off switching response of UV light irradiation (360 nm) at applied potential of 0.21 V (Fig. 5A). As shown in Fig. 5B, the oxidation peak current of DA increased with increasing pH from 6 to 7.4, but decreased with range of more than 7.4. Thus, pH 7.4 was selected as the optimum solution pH for DA sensing and is approximately the physiological pH leading to easy biological control.

Controlled surface processes of CN-SST photo-biosensor electrode were investigated in the presence of 5 µM DA using cyclic voltammetric technique under UV light irradiation (360 nm) in 0.1 M PBS (pH 7.4) at a scan rate of 100 mVs^{-1} with different scan rates ranging from 10–100 mVs^{-1}. As in Fig. 5C, the redox peaks of DA were increased with increasing scan rate, from 10 mVs^{-1} to 100 mVs^{-1}. A linear relation between oxidation and reduction peak current with the square root of scan rate was observed with regression equations I_a (µA)=2.14+0.13$v^{1/2}$ (mVs^{-1}) (R^2=0.998) and I_c(µA)=-0.927-0.1 $v^{1/2}$ (mVs^{-1}) (R^2=0.989) (Fig. 5D). This linearity suggests that the DA electrochemical process occurred at the surface of CN-SST photo-biosensor electrode is a diffusion-controlled process.[42]

Figure 4, 5

2.3 Photo-electrochemical behavior of CN-ST biosensors for monitoring mono-bioactive molecules

The photo-electrochemical performance of mono-bioactive molecules such as AA, UA, A, NA, and DA on CN-SST and SST photo-biosensor electrodes were investigated using differential pulse voltammetry in 0.1 M N_2-saturated PBS (pH= 7.4) under UV irradiation. As shown in Fig. S3(A–E). The strong DPV peak obtained from photo-electro-oxidation of AA, UA, A, NA, and DA on CN-SST photo-biosensor electrode provides the high sensitivity of designed photo-biosensor. The photo-oxidation peak potentials of 0.5 mM AA, 0.2 mM UA, 20 µMA, 20 µM NA, and 5 µM DA are at -0.01, 0.36, 0.12, 0.17, and 0.21 V in 0.1 M PBS at pH=7.4; the difference of the oxidation peak potential (peak separation) between A and NA ($\Delta E_{A\text{-}NA}$), NA and DA ($\Delta E_{NA\text{-}DA}$), and A and DA ($\Delta E_{A\text{-}DA}$) were 0.05, 0.04, and 0.9 V, respectively. The monoamine neurotransmitters have similar oxidation mechanism but slightly different in the chemical structure; their separation is very difficult but CN-SST photo-biosensor electrode provides high sensitivity toward A, NA, and DA. The peak separations of AA-DA, DA-UA, AA-UA ($\Delta E_{AA\text{-}DA}$, $\Delta E_{DA\text{-}UA}$, and $\Delta E_{AA\text{-}DA}$) were 0.22, 0.15, and 0.3 V, respectively. Thus, the ability for sensitive and selective detection of DA in

the presence of all the coexistence bioactive-molecules such as AA and UA is remarkable. Moreover, strong DPV signal obtained at low concentrations of DA compared with AA and UA might lead to superior photo-electrochemical signaling and selective discrimination of DA in biological samples.

2.4 Photo-electrochemical assays of catecholamine neurotransmitters

Monoamine neurotransmitters such as A, NA, and DA represent the catecholamine neurotransmitters and secreted with percentage values depending on its sources. The photo electro-oxidation of each molecule on CN-SST photo-biosensor electrode under UV irradiation 362 nm in 0.1 M PBS, pH 7.4 at scan rate 100 mVs^{-1}, pulse height 60 mV and pulse width 10 ms was investigated (Fig. 6). The oxidation photocurrent peak for A, NA and DA increased proportionally with increasing concentration in range from 1 µM to 32 µM with high sensitivity, indicating that the CN-SST photo-biosensor electrode can be used for the determination of A, NA, and DA. By plotting the concentration versus the current for A, NA, and DA, the linear regression equations are I(µA)= 74.31+26.7 [A](µM) (R^2=0.87), I(µA)= 75.2 + 27.8 [NA] (µM) (R^2 = 0.88), and I(µA)= 68.55+35.29 [DA] (µM) (R^2 =0.89) (Fig. 6A–6C, insets). The detection limit was calculated to be 0.11, 0.1, and 0.06 µM for A, NA, and DA. Thus, the CN-SST biosensor is sensitive for DA, NA, and A. Overall, the homogeneous charge distribution and strong binding along the electronically-coordinated structures of Ni^{2+} site, O^{2-} vacancy, and CN on the surface can dominate the retention of the actively-site surface with mobile electron clouds. The high crystallinity of original SST structures without atomic surface dissolution or aggregation leads to substantially high absorptivity of DA target. All these factors are the key role for high sensitivity and selectivity for monoamine neurotransmitters (i.e DA).

Figure 6

2.5 Photo-electrochemical selectivity of DA

Evaluation of the modified electrode for individual detection of single molecule in tertiary mixture and simultaneous detection in one pot was successfully studied using DPV in the potential range of -0.2 V to 0.7 V in N_2-saturated electrolyte (0.1 M PBS, pH 7.4) under UV irradiation 362 nm. The reactivity of individual species was observed by varying its concentration while keeping the concentration of other two species constant on the CN-SST photo-biosensor electrode. Results (Fig. S4C) showed that the DA photo-oxidation peak centered at 0.21 V (vs. Ag/AgCl) increases linearly with addition of DA doses from 1–128 µM in the presence of 0.5 mM AA and 0.2 mM UA. The regression equation was calculated by drawing a calibration plot of DA concentrations versus peak photocurrents that is given as [I (A) = 69.98 × 10^{-6}A/M [DA] + 73.78 × 10^{-6}A; R^2= 0.99; N = 5] (Fig. S4b). The detection limit was 30 nM based on regression equation (S/N = 3). Similarly, anodic peak photocurrent increases linearly from 50 µM to 400 µM, from 25 µM to 400 µM, in the presence of 10 µM DA and 0.2 mM UA or 10 µM DA and 0.5 mM AA, for AA and UA concentration injections, respectively, (Figs. S4A, and S4B, respectively). The detection range and sensitivities of the AA and UA were determined by plotting the calibration graph of concentrations versus peak currents (Figs. S4a and S4b); the peak currents are given as [I (A) = 0.8 × 10^{-6}A/M [AA] + 86.346 × 10^{-6}A; R^2= 0.99 and I (A) = 0.85 × 10^{-6}A/M [UA] + 76.6 × 10^{-6}A; R^2= 0.99; N = 5] for AA and UA, respectively. The detection limits were 12 and 9.12 µM. For further evidence, DA, AA, and UA were determined simultaneously using DPV under the latter conditions. The DPV anodic peak photocurrents show linear behavior with increasing injections of DA, AA, and UA concentrations in the range of 2–60, 25–800, and 100–1000 µM, with detection limits of 0.2, 9.78, and 11.27 µM, respectively (Figs. S4D, and S4d). Thus, the feasibility of CN-SST photo-biosensor electrode toward selective and sensitive determination of DA, AA, and UA was indicated individually or simultaneously, detecting DA in living cell even in the presence of the other interfering mono-bioactive molecules. The atomic configuration of Ni^{2+} and rich-O^{2-} vacancy sites with CN surface clouds around {110} crystal facet plane has the main reason for high DA sensitivity and selectivity at CN-SST photo-biosensor electrode, where the dominant surface charge is negative due to stabilized rich-O^{2-}. Ascorbic acid and uric acid have low pKa (5.8 and 4.2 for UA and AA) value and act as anions, whereas DA (pKa 8.9) acts as a cation at physiological pH. Repulsion between the surface of the proposed biosensor and AA and UA decrease the sensitivity due to negative repulsion. Otherwise, strong binding with DA due to the electrostatic interaction between negative surface charge and DA positive charge, which enhance the sensitivity and selectivity.[43,8]

Chronoamperometry is a highly sensitive electrochemical technique, thus it is used for screening of DA at low concentrations. Fig. 7 shows the identical current time response curve upon successive injection of 0.5 µM DA in 0.1 M PBS (pH 7.4) under UV irradiation (360 nm). High-amperometric response was observed upon addition of DA concentrations and a linear relation between the DA concentration and the reflected photocurrent was obtained. The linear regression equation was expressed as I (µA) = 3.95+28.56 [DA] (µM) (R^2 = 0.999) with signal-to-noise (S/N = 3) and %SD = 2.8%. The detection limit was calculated to be 6 nM. The lower detection limit and fast response provides that CN-SST photo-biosensor electrode is an ideal biosensor for sensitive monitoring and screening of DA.

Figure 7

3.7 Reproducibility of Photo-electrochemical sensing of DA

The reproducibility of CN-SST photo-biosensor electrode was evaluated through the photo electrochemical measurements (PEC). In such experimental protocols, the photo-current responses are examined for multiple (≥10) CN-SST biosensor electrode at a concentration of 10 µM DA at the optimum sensing conditions of 0.1 M PBS (pH 7.4) and 0.2 V (vs. Ag/AgCl) applied potential at 20 °C. The RSD of the ten amperometric response assays were in the range of 1.7% to

2.25%, as evidenced by the fitting plot of the response current graphs (Fig. S6A). To confirm reusability of CN-SST photo-biosensor electrode, the photo-current responses as a function of ten different samples with constant concentration of DA (5 μM) were measured repeatedly after every washing of CN-SST photo-biosensor electrode with distilled H_2O for three times at the optimum sensing conditions (Fig. S6B). Thus, the reused CN-SST photo-biosensor electrode showed high sensing response efficiency (i.e., 98%), despite ten reuses/cycles. These results provide high stability and reproducibility of CN-SST photo-biosensor electrode and can be assessed as significant economical sensor for monitoring of DA.

2.7 Signaling and Monitoring DA released from neuronal cells

Monitoring DA released from neuronal cells is a key in regulating both, neural mechanism and various brain functions. To demonstrate the real applicability of the developed sensor, K^+-induced dopamine released from PC12 cells were monitored through amperometric method under applied potential of 0.21 V and 0.1 M PBS at pH=7.4 in the presence of UV light irradiation (360 nm) on CN-SST photo-biosensor electrode (Figs. S5A and S5B). The cells were simulated by K^+ to depolarize the cells membrane. Cell membrane depolarization was reported by K^+ extracellular simulation in which the cell membrane depolarized and induce an influx of Ca^{2+} and Na^+ through opening of voltage-sensitive Na^+ channels and subsequent opening of voltage- sensitive Ca^{2+} channels.[44] Increasing the level of intracellular Ca^{2+} enhancing the release of dopamine from large dense-core-vesicles of the cells. The intracellular Ca^{2+} increased to threshold sufficient to trigger the exocytosis when the voltage-sensitive Ca^{2+} channel opened. Releasing of dopamine to the extracellular region expressed by K^+ induces the cell membrane depolarization and dopamine containing vesicles with cell membrane fusion. The illustration of comparability of our biosensor for monitoring of dopamine by making a control sample that contains PBS (pH 7.4) only and the other sample contains $1*10^6$ cells /mL of PC12 in 0.1 M PBS (pH 7.4) with 5 mM K^+ upon addition of DA. The high amperometric response of DA addition to both solutions with a difference in the current value was illustrated in Figs. S5 (A & B). The column in Fig. 8 shows that a difference between the current of the blank and sample contains PC12, which is corresponding to the released DA from PC12. The cellular dopamine was monitored by CN-SST photo-biosensor electrode. These results confirm that the ability of CN-SST photo-biosensor electrode for in-vitro monitoring of DA released form living cells.

Figure 8

Conclusions

A simple, sensitive, and selective biosensor was successfully developed for ultrasensitive determination of bioactive-molecules and monitoring of DA released from living cells using novel ST photo-biosensor electrodes. Building of hierarchical NiO spear thistle flower allied in single-head (S), and symmetric, asymmetric-double heads (D and A, respectively) that tightly connected through micrometric dipole-like rod or trunk were successfully fabricated. CN doped ST enhanced the intrinsic photo-electrocatalytic activity through increasing the surface area, enlarge the pore distribution, balance the surface charge (C, N, Ni^{2+}, and O^{2-} atomic configuration around {110} crystal plane with dominant O^{2-} vacancy sites and CN clouds) and improved the electrode photostability under irradiation for long-term exposure. These designated architectures are key features for generating biosensor surface electrodes for photo-electrochemical, ultrasensitive screening of mono-bioactive molecules. The exceptional electrode designs produced numerous catalytically active sites and high electron-transfer mobility. The designed photo-biosensor electrode provides significant sensitivity and selectivity for monitoring of DA among all interfered molecules such as A, UA, A, and NA. CN-SST photo-biosensor electrode showed highly photo-electrochemical activity for electrooxidation of DA at low detection limit up to 6 nM (S/N 3). Furthermore, the photo-biosensor electrode provides significant monitoring of DA from living cells (PC12). This finding indicates that the hierarchical ST biosensor can be employed for analytical discrimination and sensitive monitoring of DA released from living cells for clinical diagnosis application.

3 Experimental

3.1 Reagents

All chemicals were of analytical grade and were used without further purification. Nickel nitrate hexahydrate ($Ni(NO_3)_2.6H_2O$), diammonium hydrogen phosphate ($(NH_4)_2HPO_4$, Dopamine hydrochloride (DA), aniline, uric acid (UA), potassium ferricyanide [$K_3Fe(CN)_6$], noradrenaline (NA) and phosphate buffer saline (PBS) were purchased from Sigma–Aldrich Company, Ltd., USA. L (+)-ascorbic acid (AA) and L-adrenaline (A) were purchased from Wako Company, Ltd., Osaka, Japan. Indium tin oxide (ITO) glass electrodes (2 cm × 1 cm) were purchased from ALS Company, Ltd., Japan.

3.2 Synthesis of NiO based ST architectures

NiO was assembled with three different shapes like spear thistle (ST) flowers (ST with, single head (s), symmetric double head (D), and asymmetric double head (A by using a one-pot hydrothermal synthetic approach. In a detailed procedure, 1mM of ($Ni(NO_3)_2.6H_2O$) were dissolved in a 100 mL volumetric flask containing 50 mL deionized water and stirred until dissolved at room temperature. Next, 50 ml of 1 mM $(NH_4)_2HPO_4$ in deionized water, were added to the stirred solution of ($Ni(NO_3)_2.6H_2O$) with different flow rate (Q) to control the shape of the particles (See Scheme S1). The as prepared solution was then transferred into a 100 mL Teflon-lined stainless-steel autoclave, and was sealed and maintained at 160 °C for 8 h. After required time, green precipitates were retrieved and then rinsed with ultrapure water/absolute

ethanol to remove the soluble impurities. The as-prepared ST photo-biosensors dried in an oven at 80°C and annealed at 400 °C for 4 h to obtain ST with different morphologies.

3.3 Synthesis of NiO based CN-ST photo-biosensors

To fabricate carbon nitrogen nanosphere doped NiO based ST architectures, typically, 60 mg of prepared NiO based ST and 100 mL of tris-buffer solution (pH = 8.5) were loaded into a 250 mL volumetric flask and stirred at room temperature followed by the addition of purified aniline (20 mM). Next, 20 mM of ammonium persulphate solution was added dropwise to the stirred solution to perform the polymerization reaction at 0°C. The polymerization was preceded for 12 h at room temperature, and the obtained aniline polymerized STs were washed several times with deionized water. The polyaniline coated ST were calcined at 500 °C for 4 h in an argon atmosphere to obtain CN- ST.

3.4 Fabrication of NiO based CN-ST photo-biosensor electrodes

Working electrode fabrication was assembled as following: NiO based CN-ST architectures were dispersed in 5 ml methanol at room temperature. Thin films of CN-ST were fabricated by uniformly spreading a 15 µl onto the surface of an ITO glass substrate (2 cm × 1 cm). To control the exposed surface area of ITO substrate and for better electrical contact a definite area (1 cm × 1 cm) of the ITO electrode substrate were masked prior to the deposition. This process was repeated five times; the resulting electrode was dried overnight at room temperature, followed by washing with deionized water to remove any unbound particles.

3.5 Cell culture and in vitro study

PC12 cell line was obtained from PC12 (ATCC® CRL1721™) and was cultured by incubation under 5% CO_2 at 37 °C in Dulbecco's Modified Eagle's Medium (DMEM) containing 10% fetal bovine serum (FBS) and 10% horse serum. The culture medium was replaced every 3 to 4-day.

3.6 Photo-electrochemical measurements

Photo- electrochemical measurements (PEC) were performed with a home-built PEC system. A 500 W Xe lamp equipped with monochromator was used as irradiation source. Photocurrent was measured on Zennium/ZAHNER-Electric instrument that was controlled by Thales Z 2.0 software at room temperature. A conventional three-electrode system containing ITO glass modified (2 cm × 1 cm) as working electrodes, platinum wires as counter electrode, and Ag/AgCl (3 M NaCl) as reference electrode was used for electrochemical analysis. The freshly prepared electrolyte (0.1 M PBS (pH 7.4)) was de-aerated by bubbling a slow stream of purified N_2 to avoid dopamine oxidation. The N_2 flow was maintained during the entire electrochemical measurements to ensure N_2-saturated electrolyte.

References

1 C. Riether, C. M. Schurch and A. F. Ochsenbein, *Cell death and differentiation,* 2015, **22 (2)**, 187-198.
2 C. Aicheng and C. Sanghamitra, *Chem. Soc. Rev.,* 2013, **42 (12),** 5425-5438.
3 B.-R. Li, Y.-J. Hsieh, Y.-X. Chen, Y.-T. Chung, C.-Y. Pan, Y.-T. Chen, *J. Am. Chem. Soc.,* 2013, **135 (43)**, 16034-16037.
4 X. Zhang, et al., *Anal. Chem.*, 2015, **87 (6)**, 3360-3365.
5 E. Farjami, R. Campos, J. S. Nielsen, K. V. Gothelf, J. Kjems and E. E. Ferapontova, *Anal. Chem*., 2013, **85**, 121–128.
6 J. S. Huang, Y. Liu, H. Q. Hou and T. Y. You, *Biosens. Bioelectron.*, 2008, **24**, 632–637.
7 T. Nakaminami, S.F. Ito, S.F. Kuwabata, H. Yoneyama, *Anal. Chem.* 1999, **71**, 1928-1934.
8 E. Popa, Y. Kubota, D.A. Tryk, A. Fujishima, *Anal. Chem*., 2000, **72,** 1724–1727.
9 J.-M. Zen, P.-J. Chen, *Anal. Chem*., 1997, **69**, 5087–5093.
10 Y.X. Li. and X.Q. Lin, *Sens. & Actuat. B: Chem.*, 2006, **15(1),** 134-139.
11 Y. Zeng, C. Li, C. Tang, X. Zhang, G. Shen and R. Yu, *Electroanalysis*, 2006, **18**, 440–448
12 D. Bruns, et al., *Methods*, 2004 **8;33(4)**, 312-21.
13 N.F. Atta, M.F. El-Kady and A. Galal, *Sens. Actuat. B: Chem.*, 2009, **141(2),** 566-574.
14 P. Kalimuthu and S.A. John, *Bioelectrochemistry*, 2009, **77(1)**, 13–18.
15 X. Zhang, W. Yan, J. Zhang, Y. Li, W. Tang and Q. Xu, *RSC Advances*, 2015, **5**, 65532-65539.
16 W. Cai, J. Lai, T. Lai, H. Xie, J. Ye, *Sensors and Actuators B*: *Chemical*, 2016, **224,** 225–232.
17 X. Zhang, Y.-C. Zhang and L.-X. Ma, *Sensors and Actuators B: chemical*, 2016, **227,** 488–496
18 G.-L. Wang, J.-J. Xu and H.-Y. Chen, *Biosensors and Bioelectronics*, 2009, **24**, 2494–2498.
19 W.W. Zhao, Z.Y. Ma, P.P. Yu, X.Y. Dong, J.J. Xu and H.Y. Chen, *Anal. Chem.,* 2012, **84,** 917–923.
20 W.W. Tu, J.P. Lei, P. Wang and H.X. Ju, *Chem. Eur. J*., 2011, **17,** 9440–9447.
21 W.W. Tu, Y.T. Dong, J.P. Lei and H.X. Ju, *Anal. Chem.*, 2010, **82**, 8711–8716.
22 H.J. Chen and L.Z. Wang, *Beilstein J. Nanotech*., 2014, **5,** 696–710.
23 K. Wang, J. Wu, Q. Liu, Y.C. Jin, J.J. Yan and J.R. Cai, *Anal. Chim. Acta*, 2012, **745**, 131–136.
24 Y. Li, Y. Hu, Y. Zhao, G. Shi, L. Deng, Y. Hou and L. Qu, *Adv. Mater.*, 2011, **23,** 776–780.
25 B. Sun, K. Zhang, L.J. Chen, L.T. Guo and S.Y. Ai, *Biosens. and Bioelect.,* 2013, **44,** 48–51.
26 X.M. Zhao, S.W. Zhou, L.P. Jiang, W.H. Hou, Q.M. Shen and J.J. Zhu, *Chem. Eur. J*, 2012, **18,** 4974–4981.
27 T.T. Duong, Q.D. Nguyen, S.K. Hong, D. Kim, S.G. Yoon and T.H. Pham, *Adv. Mater.*, 2011, **23,** 5557–5562.
28 X. Zhang, F. Wang, H. Huang, H.T. Li, X. Han, Y. Liu and Z.H. Kang, *Nanoscale*, 2013, **5**, 2274–2278.
29 F. Vietmeyer, B. Seger and P.V. Kamat, *Adv. Mater.*, 2007, **19,** 2935–2940.
30 Y. Yan, Q. Liu, X. Du, J. Qian, H. Mao, K. Wang, *Anal. Chim. Acta*, 2015, **853**, 258-264.
31 Y. Yang, K. Yan and J. Zhang, Electrochimica Acta, 2017, **228**,28-35.
32 H. Lia, J. Lia, D. Chenb, Y. Qiua and W Wang, *Sens. Actuat. B*: chem., 2015, **220**, 441–447.
33 Y. Wang, C. Gao, S. Ge, J. Yu and M. Yan, *Biosens. Bioelectro.*, 2016, **85**, 205–211.
34 K. S. W. Sing, D. H. Everett, R. A. W. Haul, L. Moscou, R. A. Pierotti, J. Rouquérol and T. Siemieniewska, *Pure Appl. Chem.*,1985, **57**, 603−619.

35 X. Bo, J. Bai, J. Ju and L. Guo, *J. Power Sources,* 2011, **196**, 8360–8365.
36 T. Kavitha and H. Yuvaraj*, J. Mater. chem*., 2011, **21(39)**, 15686-15691.
37 W. Liu, Y. Feng, X. Yan, J. Chen and Q. Xue, *Adv. Funct. Mater*., 2013, **23**, 4111-4122.
38 S. Y. Kim, H. M. Jeong, J. H. Kwon, I. W. Ock, W. H. Suh, G. D. Stucky, J. K. Kang, *Energy Environ. Sci.*, 2015, **8**, 188-194.
39 S. A. El-Safty, Y. Kiyozumi, T. Hanaoka and F. Muzukami, *Appl. Catal. B: Environ.,* 2008, **82**, 169-179.
40 D. H. Shin, J. S. Lee, J. Jun and J. Jang, *J. Mater. Chem., A* 2014, **2**, 3364-3371.
41 L. Chen, M. Feng and H. Zhan, *RSC Adv.,* 2014, **4**, 30689-30696.
42 R. Nurzulaikha, H.N. Lim, I. Harrison, S.S. Lim, A. Pandikumar, N.M. Huang, S.P. Lim, G.S.H. Thien, N. Yusoff and I. Ibrahim, *Sensing and Bio-Sensing Research*, 2015, **5,** 42–49
M. Ghita and D.W.M. Arrigan, Electrochimica Acta*,* 2004, **49(26)**, 4743-4751.
43 H. Shinohara, Y. Sakai and T.A. Mir, *Anal. Biochem.*, 2013, **441**,185–189.

Figures

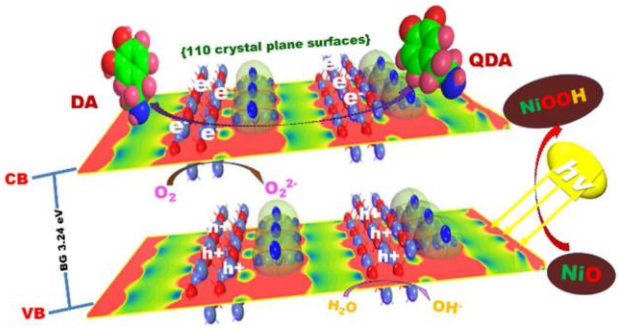

Scheme 1. represent the process of photo-electrooxidation of dopamine on the surface of {110} crystal plane with atomic configuration of $Ni^{2+}$and O^{2-} along with clouds of CN and the effective charge transfer at the surface with formation of active sites from rich-vacancies O^{2-} and Ni^{2+}.

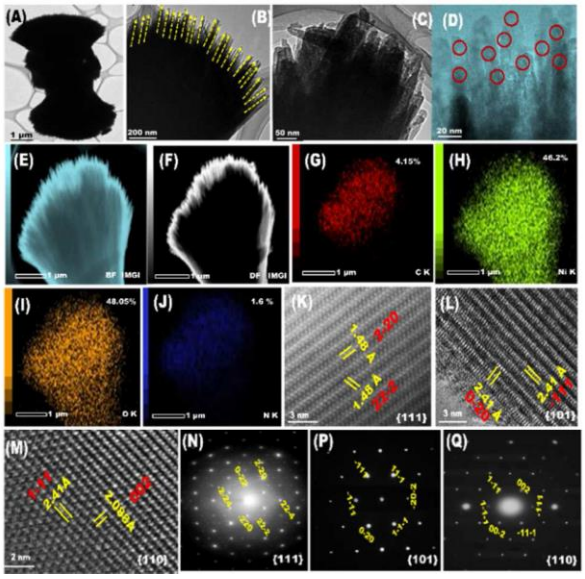

Figure 1. A) low magnification HR-TEM micrograph illustrates the surface morphology of one of the designed ST with two heads connected by trunk which is like spear thistle (ST) flowers with double head (DST). High magnification of HAADF-STEM reflects the head morphology that is like a thick serrated surface as in (B). c) HAADF-STEM photograph reflects the head serrated surface consists of a thick nanotube with average size around 20 nm. (D) shows high magnified HAADF-STEM image focused on the nanotube surface and obtained the CN formatted at the surface of ST with average size > 2nm and covers the surface with formality and homogenously. Confident STEM mapping obtaining the homogeneous dispersion of C, Ni, O, Ni at the prepared CN at ST samples as in (E-I). (K-M) High magnification HAADF-STEM of ST architectures which reflected the degree of crystalline surface. High-dense {111}-ED-STEM (L) for symmetric double head, {101} for asymmetric double head, and {110} for single head. micrographs of root- and top- sides of ST samples and the corresponding atomic configuration along with {111}, {101} and {110} crystal planes for symmetric double head, asymmetric double head and single head, respectively.

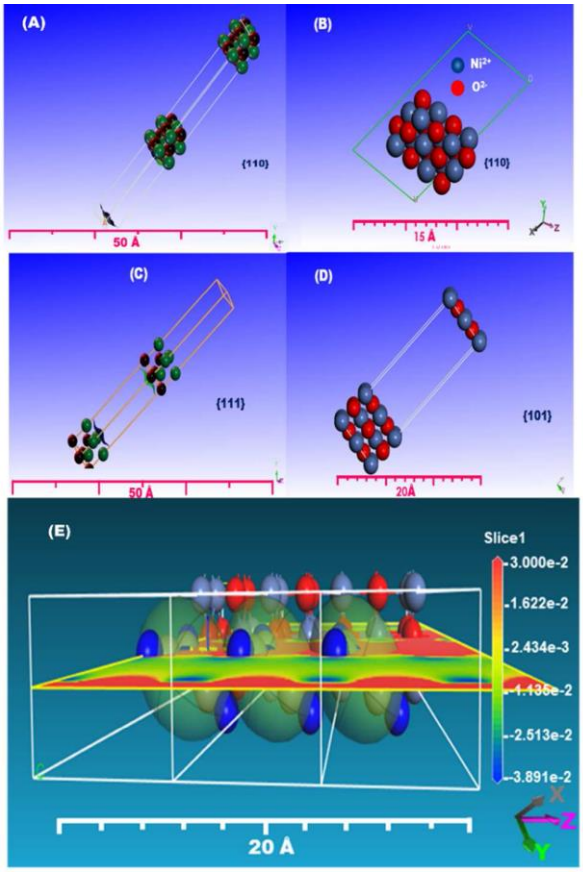

Figure 2. A) the top-view of double layer ST atomic organization along with {110} crystal plane for SST and demonstrated the Ni^{2+} and O^{2-} configuration with highly order crystalline surface. B) the atomic arrangement of Ni^{2+} and O^{2-} as monolayer based on axial alignment and represents the low contact angel between the target molecules and atomic active centers, which affect on the catalytic behavior of {110} plane. C and D) top view of double layer of atomic configuration around {111} and {101} crystal plane for DST and AST, respectively. E) top view of multi-layer of atomic arrangement around {110} crystal facet plane along with providing CN. The orientation of building atomic tower shows

the possibility of the {110}- top-surface binding sites with high densely electronic clouds with the crystal edge surface and central crystal corresponding to density functional theory (DFT) with effectiveness of CN on the surface atomic construction and its contact with the biomolecules.

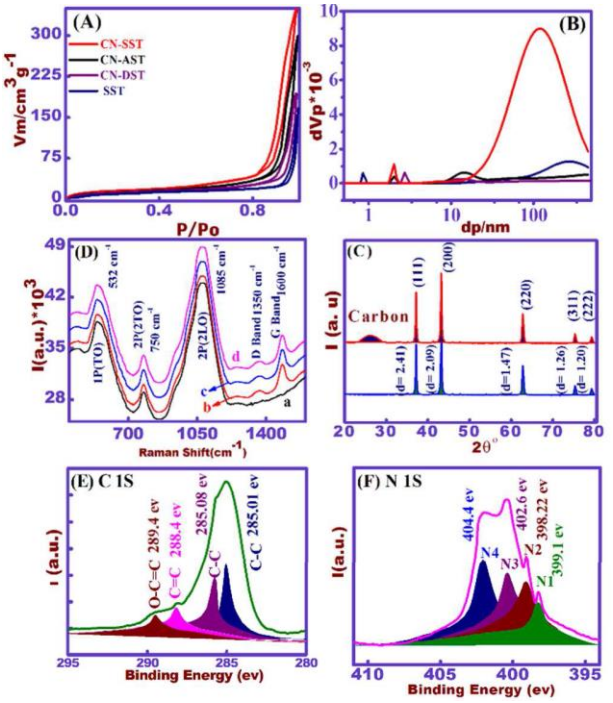

Figure 3. A) N_2 isotherms of the ST without and with CN of DST, AST and SST, which featured type IV isotherm H1-type hysteresis loop. B) NLDFT model for pore size distribution, inset table contains the data of surface area, pore size and pore volume and (C) WA-XRD pattern of SST (blue line) and CN-SST (red line). (D) Raman spectrum of SST (a) CN-DSH (b), CN-AST (c) and CN-SST (d). XPS Survey of CN-SST samples; (E) C 1S, (F) N 1s.

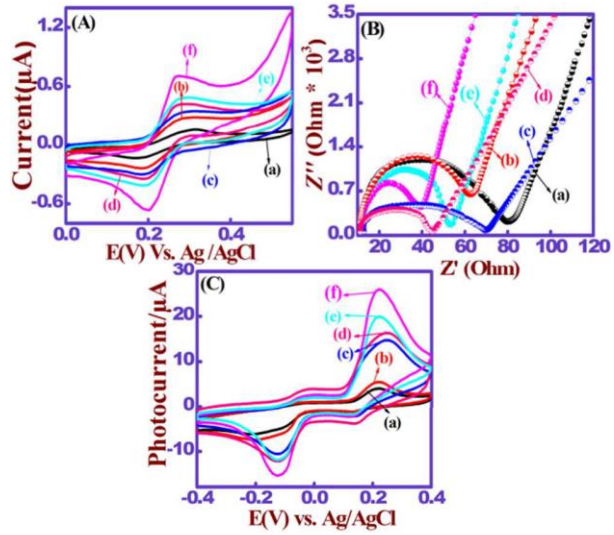

Figure 4. (A) CVs of DST & CN-DST(a, b), AST & CN-AST (c, d) and SST & CN-SST (e, f) photo biosensor electrodes in 0.1 M PBS (pH =7) containing 0.1 mM of $[Fe(CN)_6]^{3-}$ at 100 mVs^{-1}, (B) Electrochemical impedance of DST & CN-DST(a, b), AST & CN-AST (c, d) and SST & CN-SST (e, f) photo biosensor electrodes in 0.1 M PBS (pH = 7) and (C) CVs of DST & CN-DST(a, b), AST & CN-AST (c, d) and SST & CN-SST (e, f) photo biosensor electrodes in 0.1 M PBS pH=7.4 containing 10 μM of DA at scan rate 100 mVs^{-1} under UV irradiation (360 nm).

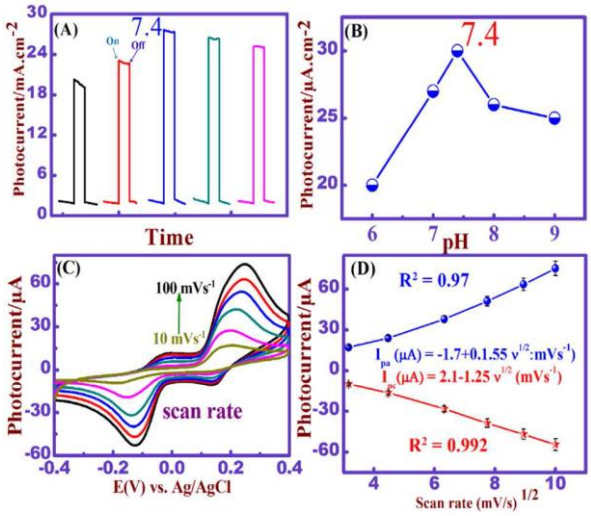

Figure 5. (A) time –dependent on-off switching response CN-SST photo biosensor electrode in PBS containing 10 μM dopamine with varying pH from 6 to 9 under UV light irradiation (360 nm) at applied potential 0.21 V, (B) the plot of pH versus the photocurrent (μA), (C) CVs of 10 μM dopamine in PBS pH =7.4 at different scan rate from 50- 300 mVs^{-1} under UV light irradiation and (D) the linear plot of square root of scan rate versus anodic and cathodic photocurrent (μA).

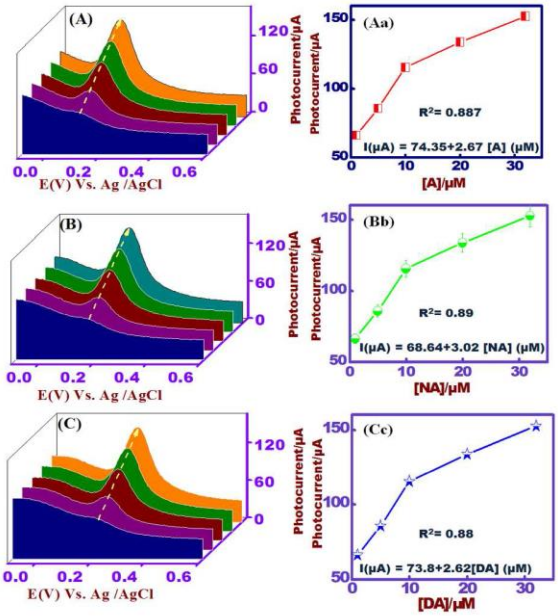

Figure 6. DPV of 1, 5, 10, 20 and 32 μM of A (A), NA (B) and DA (C) under UV light irradiation (360 nm) in 0.1 M PBS pH=7.4. (Aa), (Bb) and (Cc) the linear plot of concentration (μM) Vs the photocurrent (μA) for A, NA and DA, on CN-SST photo biosensor electrode, respectively.

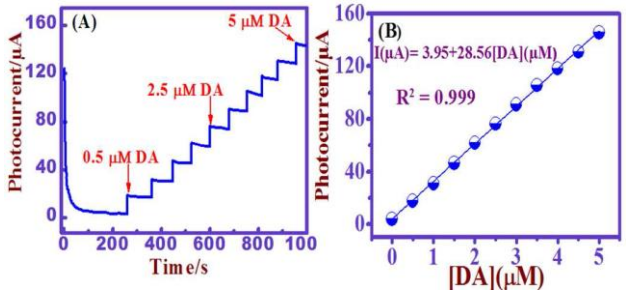

Figure 7. Amperometric response of DA with successive addition of each step 0.5 µm under UV light irradiation (360 nm) in PBS pH=7.4 and applied potential 0.21V, (B) the linear plot of concentration (µM) Vs the photocurrent (µA) on CN-SST photo biosensor electrode

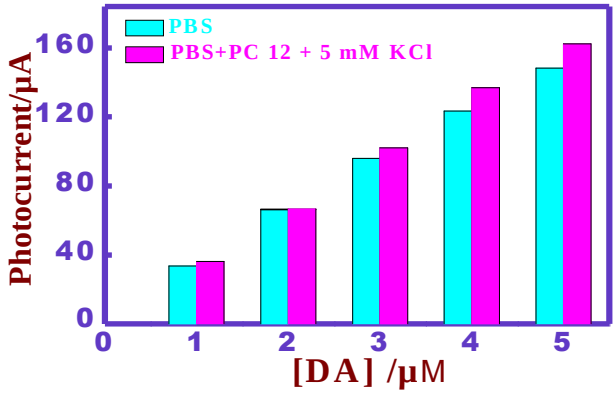

Figure 8. The column plot of concentration of dopamine with (red column) and without (blue column) PC12 (5 mM KCl) Vs the Photocurrent (µA) µm under UV light irradiation (360 nm) in 0.1 M PBS pH=7.4 on CN-SST photo biosensor electrode.

Supplementary

Photo-electrochemical biosensor for ultrasensitive screening of mono-bioactive molecules in living cells

N. Akhtar[a,b], M. Emran[a], M. A. Shenashen[a], , T. Osaka [b], A. Faheem [c], T. Homma [b], H. Kawarada [b*], S. A. El-Safty[a,b,*]

Characterization analyses

The morphologies of the annealed samples were investigated by FE-SEM (JEOL Model 6500) at 20 kV. Analysis material was fixed onto the FE-SEM stage using carbon tape before insertion into the FE-SEM chamber. The ion sputter (Hitachi E-1030) was used to deposit thin-layered Pt films on electrodes at 25 °C.

A focused ion beam (FIB) system (JEM-9320FIB) operated at accelerating voltages from 5–30 kV with variable steps of 5 kV and magnification ranging from 150× to 300000×. The orientation axis (X and Y) of the powder samples containing NiO with different morphological structures CN-STC-N can be changed within ±1.2 mm through a tilt angle of ± 60°. The samples were inserted inside the FIB machine using a bulk-sample holder (8 × 8 mm^2) after deposition by a carbon protection layer. Before FIB investigation, the powder samples of the NiO with different morphological structures CN-STC-N were mixed with small amounts of epoxy (Gatan, Inc.) onto a small silicon wafer using a fine eyelash probe to form very thin films on the silicon. Each thin film was backed on a hot plate at 130 °C for 10 min and subsequently coated with a uniformly thin carbon layer of about 30 nm. The samples were inserted into the FIB microscope operated at 30 kV and then roughly milled on both sides until a final thickness of 2 μm using −1.5° and +1.5° tilts. Afterward, the NiO with different morphological structures CN-STC-N were cut and removed from the FIB system for subsequent HR-SEM analysis.

High-resolution transmission electron microscopy (HRTEM), electron diffraction (ED), scanning transmission electron microscopy (STEM), and energy dispersive X-ray spectroscopy for elemental mapping (STEM-EDS) were performed using a JEOL JEM model 2100F microscope. HRTEM was conducted at an acceleration voltage of 200 kV to obtain a lattice resolution of 0.1 nm and the spherical aberration of 1.0 mm. The HRTEM, STEM and STEM-EDS were operated at a camera length of 20 and a spot size of 1 nm. STEM and STEM-EDS

were carried out at a camera length of 40 cm and a spot size of 0.7 nm. In the HRTEM, ED, STEM, and STEM-EDS characterization, the samples were dispersed in ethanol solution using an ultrasonic cleaner, and then dropped on a copper grid. Prior to inserting the samples into the HRTEM column, the grid was vacuum dried for 20 min.

The surface properties of the material involving the pore structure distribution and surface area were estimated by N_2 adsorption–desorption isotherms at 77 K using a BELSORP36 analyzer (JP. BEL Co., Ltd.). The samples were thermally treated at 200 ℃ for at least 6 h under N_2 atmosphere. The specific surface area (SBET) was calculated using the Brunauer–Emmett–Teller (BET) method with multipoint adsorption data from the linear section of the N_2 adsorption isotherm. The pore size distribution was determined using nonlocal DFT (NLDFT).

The structural geometry of the catalysts was further examined by WA-XRD. The WA-XRD patterns were recorded using a 18 kW diffractometer (Bruker D8 Advance) at scan rate of 10°/min with monochromated CuKα-X-radiation (λ = 1.54178 Å). The DIFRAC plus Evaluation Package (EVA) software with the PDF-2 Release 2009 databases provided by Bruker AXS was used to analyze the diffraction and structure analysis diffraction data. The TOPAS package program was applied to integrate various types of X-ray diffraction (XRD) analyses.

XPS analysis was conducted on a PHI Quantera SXM (ULVAC-PHI) instrument (Perkin–Elmer Co., USA) equipped with Al Kα as an X-ray source for excitation (1.5 mm × 0.1 mm, 15 kV, 50 W) under a pressure of 4×10^{-8} Pa. A thin film of the sample was deposited on a Si slide before the start of analysis.

Raman spectroscopy (HR Micro Raman spectrometer, Horiba, Jobin Yvon) was conducted using an Ar ion laser at 633 nm. A CCD (charge coupled device) camera detection system and the LabSpec-3.01C software package were used for data acquisition and analysis, respectively. To ensure the accuracy and precision of the Raman spectra, 10 scans of 5 s from 300 cm^{-1} to 1,600 cm^{-1} were recorded.

Scheme S1. The schematic synthesis approach of SST, DST and AST within addition of 15 mL of 1 Mm $(NH_4)_2HPO_4$ with controllable rate (Q).

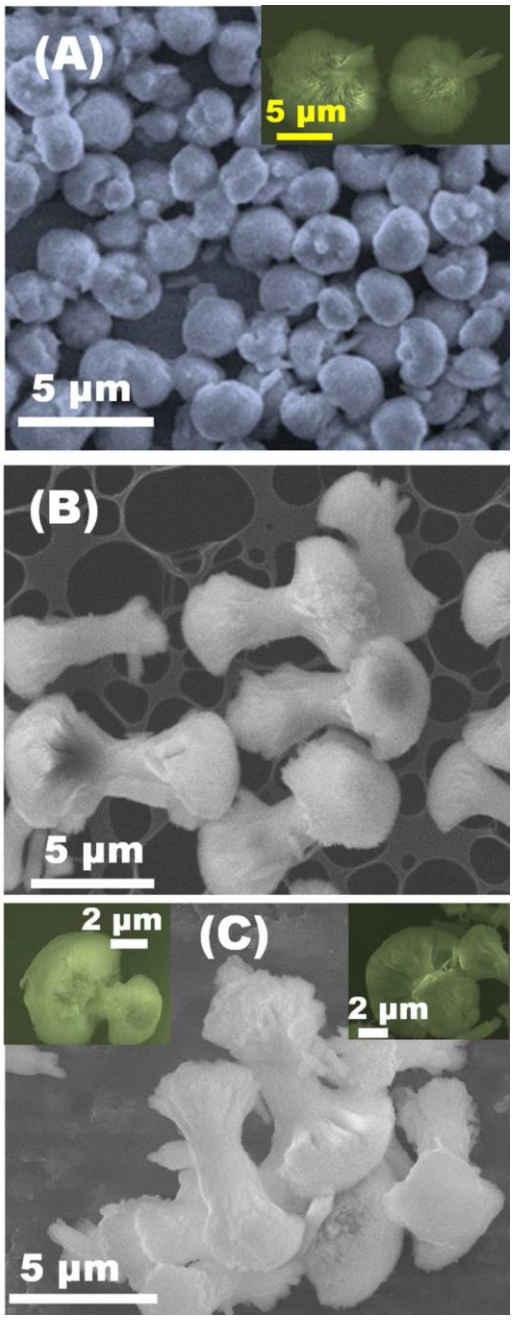

Figure S1 A) low magnification of FE-SEM shows the morphology of CN-SST which is like spear thistle (ST) with head and trunk, inset; high magnification FE-SEM of CN-SST. B) FE-SEM micrograph of ST with two symmetric head connected by rod in-between (CN-DST). C)low magnification of FE-SEM obtains the ST morphology which is like a spear thistle (ST) with two asymmetric head, and its inset high magnification of CN-AST unit.

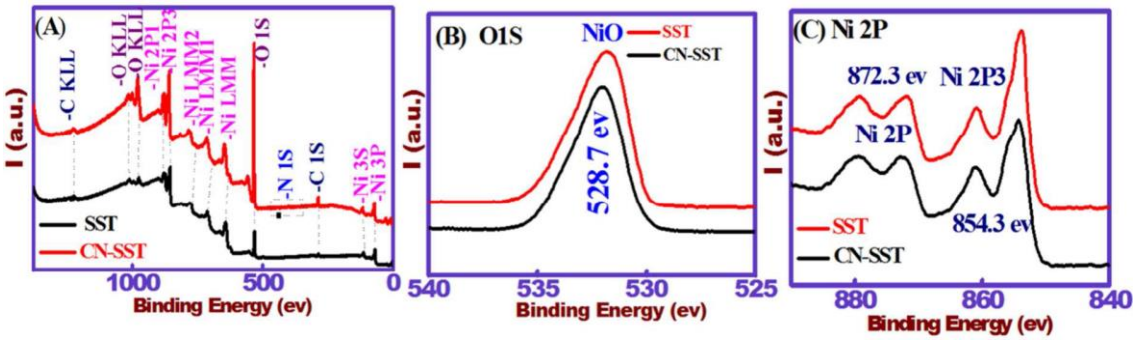

Figure S2. (A) XPS spectra of ST and CN-SST spheres and Survey of the samples; (B) O 1S and (C) Ni 2P.

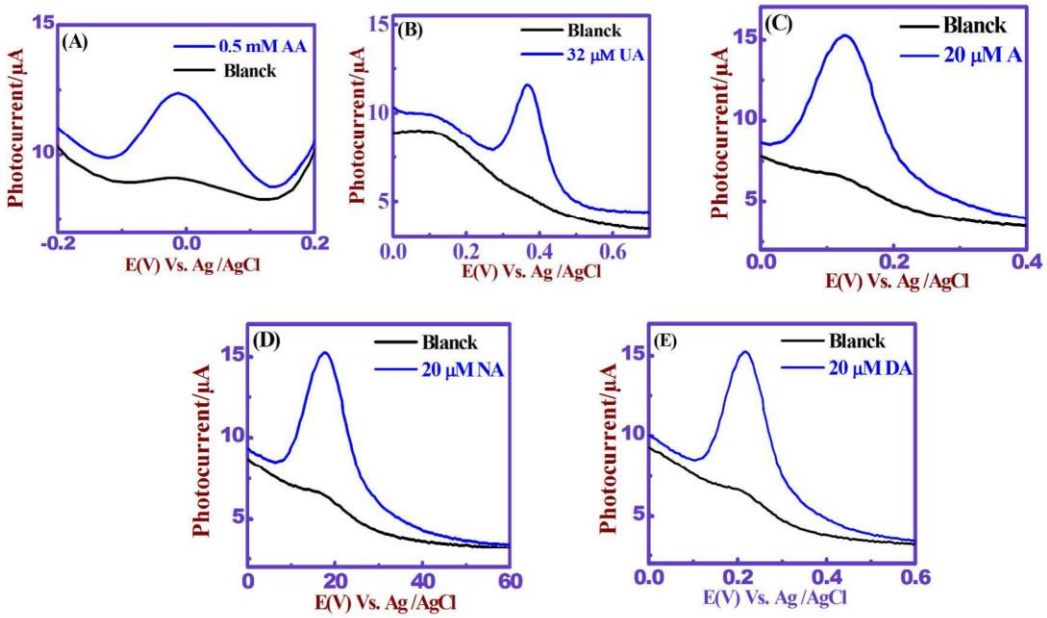

Figure S3. DPV of 0.5 mM AA (a), 32 μM UA(b), 20 μM A(c), 20 μM NA(d) and 20 μM DA (e) at CN-SST photo-biosensor electrode under UV light irradiation (360 nm) in 0.1 M PBS pH=7.4.

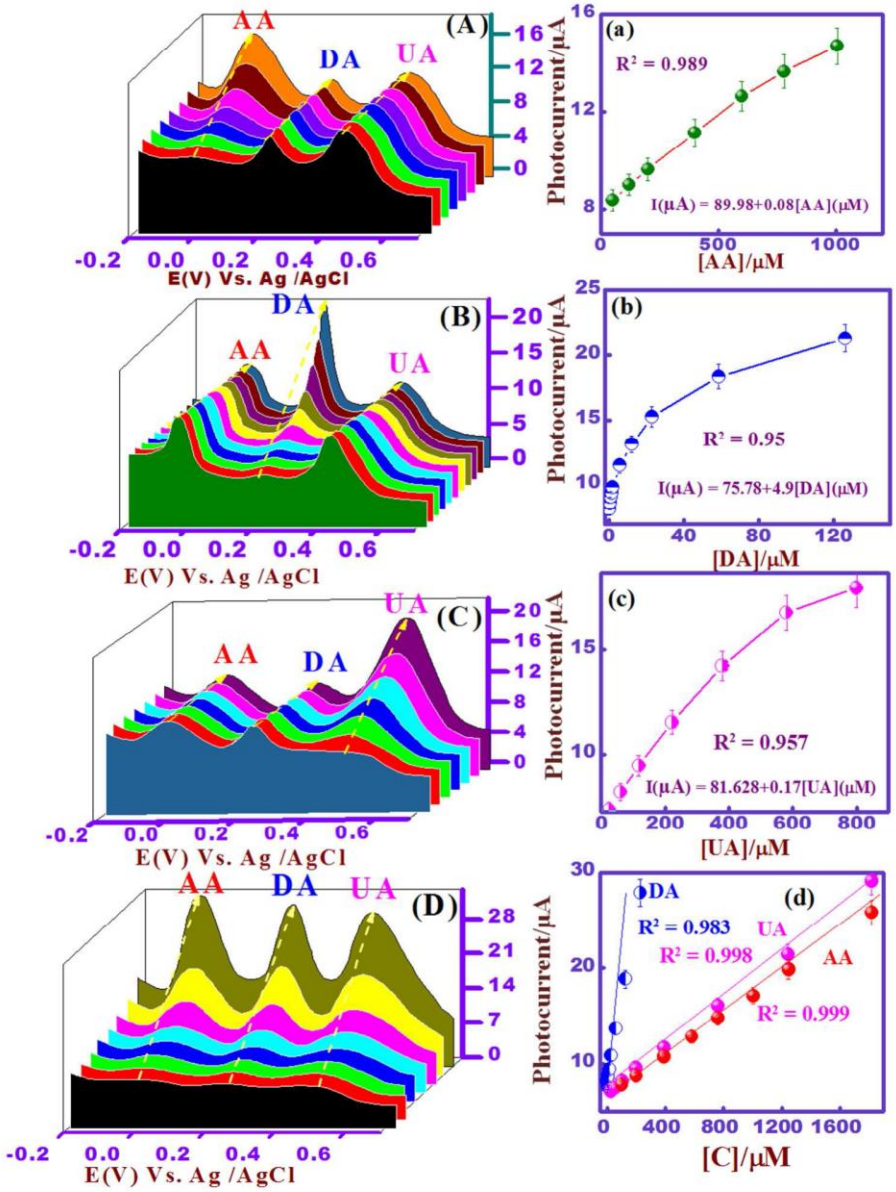

Figure S4. DPV curves at, (A) increasing concentrations of AA (50-1000 μM) in the presence of 10 μM DA and 0.2 mM UA (a) the plot of concentration of AA (μM) versus current (μA) , (B) increasing concentrations of DA (0.1-125 μM) in the presence of 0.5 mM AA and 0.2 mM UA, (b) the plot of concentration of DA (μM) versus current (μA), (C) increasing concentrations of UA (25-800 μM) in the presence of 10 μM DA and 0.5 mM AA, (c) the plot of concentration of DA (μM) versus current (μA) and (D) increasing concentrations of AA (25-1800 μM), DA (2-225 μM) and UA (100-1800 μM), (d) the plot of concentration of AA, DA and UA (μM) versus current (μA) simultaneously under UV light irradiation (360 nm) in 0.1 M PBS (pH 7.4) on CN-SST photo-biosensor electrode.

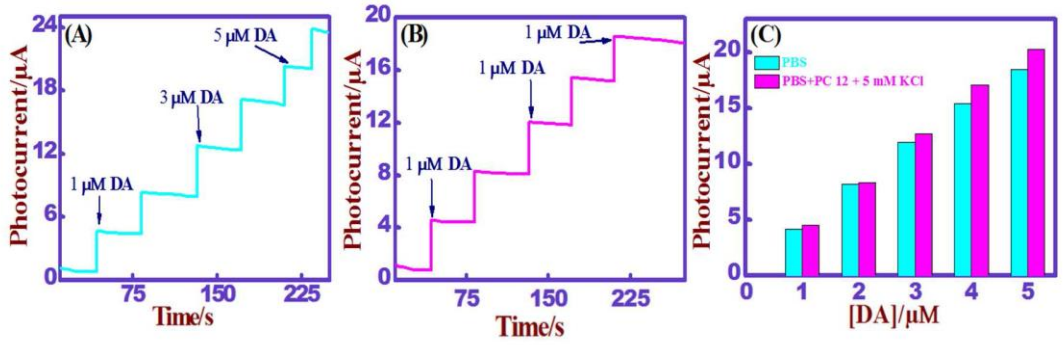

Figure S5. amperometric response of dopamine addition in PBS pH=7.4 without (A) and with PC 12 induced by 5 mM KCl (B). the column plot represents the concentration of dopamine with (magenta column) and without (cyan column) PC12 (5 mM KCl) Vs the photocurrent current (μA) under UV light irradiation on CN-SST photo-biosensor electrode.

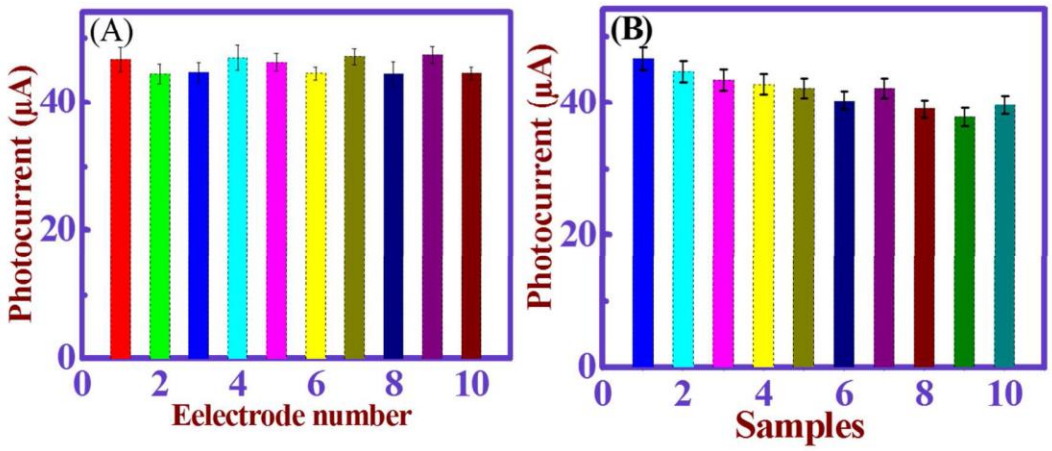

Figure S6. The columns of the reproducibility (A) of CN-SST photo-biosensor electrode of 10 different electrodes to 5 μM DA. Reusability (B) of CN-SST photo-biosensor electrode for 10 samples with constant concentration of DA (5 μM) μm under UV light irradiation in PBS pH=7.4.